Separation and Purification Technology 390 (2026) 136718

Contents lists available at ScienceDirect

Separation and Purification Technology

journal homepage: www.elsevier.com/locate/seppur

Defect-engineered Mn–Fe_2O_3 catalysts enable heterogeneous Fe^{IV}=O formation for enhanced Fe(VI)/H_2O_2 oxidation of organic pollutants

Zhengming He [a], Cong Li [a,*], Jingzhen Su [a], Kai Zhang [a], Qiufeng Lin [b], Jiaxue Zhu [a], Hyunook Kim [c], Jieming Yuan [a], Yun Li [d]

[a] School of Environment and Architecture, University of Shanghai for Science and Technology, Shanghai 200093, China
[b] Department of Civil & Architectural Engineering, University of Miami, United States
[c] Department of Environmental Engineering, University of Seoul, South Korea
[d] Guangxi Minzu University, China

ARTICLE INFO

Keywords:
Oxygen vacancy
Hypervalent iron-oxo
Fe(VI)
H_2O_2

ABSTRACT

Iron-based catalysts are generally used to activate oxidizing species, such as hydrogen peroxide by increasing homogeneous active substances like free radicals, to promote the degradation of organic matter. However, less attention has been paid to the reactions on the surface or the generation of heterogeneous metal-oxo species. Herein, oxygen vacancies (Vo) were introduced into Fe oxides by a calcination-induced hetero-atom doping modification. The characteristic peak of the heterogeneous hypervalent iron-oxo [≡Fe^{IV}=O] species in the UV–Vis spectrum at 371 nm was observed. In the context of electrochemical experiment, Vo-rich Mn-Fe_2O_3 significantly enhanced the electron conduction of sulfamethoxazole and H_2O_2, while simultaneously inhibiting the self-decomposition of potassium ferrate (Fe(VI)). Regarding the H_2O_2 generated during the self-decomposition process of Fe(VI), Vo-rich Mn-Fe_2O_3 can accelerate the degradation of sulfamethoxazole, increasing the reaction rate to 0.1081 min^{-1} (with a 30.05 % improvement in removal efficiency). Density functional theory calculations indicate that Vo leads to an enhanced capture of O atoms by the low-coordinated Fe atoms, promoting the anchoring of H_2O_2 and the formation of the active ≡Fe^{IV}=O with a higher spin state. This work proposes heterogeneous reactive species on the surface of metal oxidase, constructing Vo as the O atom capture sites in iron-based oxides to facilitate the formation of ≡Fe^{IV}=O and the degradation of organic compounds.

1. Introduction

For the remediation of trace and refractory pollutants in water, the advanced oxidation processes (AOPs) in wastewater treatment are gaining increasing attention due to their excellent degradation capacity. Owing to its stronger ability to capture electrons in aqueous phases with protonation increasing [1], ferrate (Fe(VI)) possesses a powerful oxidation capacity, which has been demonstrated in organic matter degradation [2]. Considering the remarkable oxidation capacity of hypervalent iron (Fe(IV)) and Fe(V)) species, the exploration of pathways for the activation or catalysis of Fe(VI) has been further advanced. This is achieved through the utilization of transition metal ions in low or intermediate valence states [3], heterogeneous catalysts such as layered double hydroxide particles [4,5], colloid transition metal oxides [6,7] , and even nanoscale zerovalent iron [8]). Most of these activations accelerate the oxidation of organic matter by stimulating the production of Fe(V) and Fe(IV) from the reduction of Fe(VI), which could produce H_2O_2 in this process [9]. However, the oxidation capacity of H_2O_2 produced by the self-decomposition of hypervalent iron is less than that of Fe(V) and Fe(IV) and has rarely received comparable attention in Fe (VI) system [10]. Furthermore, the iron particles produced during this process have attracted even less attention.

Inspired by those natural enzymes using porphyrins or delicate ligands to heterolytically generate the Fe-oxo species [11,12], ferric oxides have demonstrated strong catalytic performance in oxygen-atom transfer reactions, leading to the formation of Fe–oxo species with notable oxidative capacity [13]. Heterogeneous catalysts prepared by doping iron with manganese have also shown great potential for

* Corresponding author.
E-mail addresses: zhengming-he@foxmail.com (Z. He), licong@usst.edu.cn (C. Li), sjzhen98@foxmail.com (J. Su), Kevin_ZhangK@126.com (K. Zhang), qxl398@miami.edu (Q. Lin), zhuxile521@163.com (J. Zhu), h_kim@uos.ac.kr (H. Kim), liyun@gxmzu.edu.cn (Y. Li).

https://doi.org/10.1016/j.seppur.2025.136718
Received 8 September 2025; Received in revised form 5 December 2025; Accepted 30 December 2025
Available online 31 December 2025

activating peroxymonosulfate (PMS) and H_2O_2 [14,15]. This enhanced activity is attributed to oxygen vacancies (Vo) on metal oxide surfaces [7]. The doping of elements with similar atomic radius can easily cause lattice distortion, thereby facilitating the formation of Vo [16]. Previous studies have confirmed the formation of heterogeneous $\equiv Fe^{IV}=O$ species on the surface of iron-based catalysts with hetero-atomic doping, which efficiently active H_2O_2 or other oxidizing agents [17–19]. Therefore, it is desirable to explore the catalytic performance of Mn-doped Fe oxides for H_2O_2 generated during the self-decomposition of Fe(VI).

In this study, Vo-rich Mn-Fe_2O_3 was constructed from iron oxides and manganese oxides via calcination in an oxygen-poor atmosphere. The oxidation selectivity of Fe(VI) and H_2O_2 toward aromatic compounds with different functional groups, mediated by the Vo-rich Mn-Fe_2O_3 catalyst, was systematically investigated to advance the mechanistic understanding of heterogeneous reactions in AOPs. The catalytic mechanisms of Vo-rich Mn-Fe_2O_3 in the Fe(VI) and H_2O_2 system were elucidated by evaluating its catalytic activity, dominant reactive species and electron-transfer efficiency. The presence of $\equiv Fe^{IV}=O$ on the surface of the catalyst was confirmed by spectroscopy and its formation process was further analyzed via density functional theory (DFT). This work proposed a feasible strategy to exploit defect-engineered iron-based oxides for catalyzing Fe(VI) and H_2O_2 reactions in AOPs.

2. Materials and methods

2.1. Reagents

Iron(III) nitrate nonahydrate ($Fe(NO_3)_3{\cdot}9H_2O$, 99.99 %), manganese (II) nitrate tetrahydrate ($Mn(NO_3)_2{\cdot}4H_2O$, 99.99 %), sulfamethoxazole (SMX), potassium hydroxide (KOH), acetonitrile, phosphoric acid, horseradish peroxidase (HRP), 2,2′-Azinobis-(3-ethylbenzthiazoline-6-sulphonate) diammonium salt (ABTS), bisphenol A (BPA), p–Nitrophenol (p-NP), phenol, acetaminophen (AcP), aniline, benzaldehyde 2,4–hexadiene (2,4-HD), tert-butyl alcohol (TBA), p-benzoquinone (PBQ), furfuryl alcohol (FAA) and methanol were all purchased from Shanghai Aladdin Biochemical Technology Co., Ltd. All chemicals were of analytical grade and used as received. H_2O_2 (30 %) was obtained from Sinopharm Chemical Reagent Co., Ltd. Fe(VI) was synthesized in the laboratory with a purity of over 90 % [20]. The water during experiments was ultrapure with a resistivity of 20 MΩ.

2.2. Preparation of Mn-Fe_2O_3 catalysts

The Mn-Fe_2O_3 catalyst was prepared by the coprecipitation method. First, 100 mL of a 600 $g{\cdot}L^{-1}$ KOH solution was prepared by dissolving 60 g of KOH under magnetic stirring for 2 h, followed by thorough cooling to maintain a highly concentrated alkaline solution. Subsequently, at a temperature below 5 °C, 5.19 g of $Fe(NO_3)_3{\cdot}9H_2O$ and 19.37 g of $Mn(NO_3)_2{\cdot}4H_2O$ were slowly added to the strong alkaline solution under rapid stirring to ensure complete dissolution.

The solids obtained were filtered and washed 3 times with deionized water, followed by drying in a constant-temperature air oven at 105 °C for 24 h. A portion of the dried powder was then transferred into a quartz boat and placed in a tube furnace. Nitrogen was purged for 30 min to remove most of the residual air. Calcination was performed by heating the sample to 700 °C at a rate of 5 °C·min^{-1}, maintaining this temperature for 4 h, and subsequently allowing the sample to cool naturally to room temperature. The ground product was denoted as Mn–Fe_2O_3–700. When the material was used without high-temperature calcination (maintained under 25 °C), the ground product was considered as Mn–Fe_2O_3–25.

2.3. Characterization

The X-ray diffractometer (XRD, D8 Advance, Bruker) equipped with Cu-Kα radiation at a scanning rate of 2° min^{-1} over the range of 10°-90° (2θ) was utilized to measure the crystalline structure and phase purity. Oxygen vacancy in the Mn–Fe_2O_3 catalysts were characterized by room-temperature electron paramagnetic resonance (EPR, A300, Bruker), and radical signals were recorded in the absence of quenching agents. Nitrogen sorption isotherm experiments of Mn-Fe_2O_3–25 and Mn-Fe_2O_3–700 samples by the method of Brunauer-Emmett-Teller (BET) with a QuadraSorb SI automated surface area and pore size analyzer (Quantachrome Instruments) at 77 K. The Mn-Fe_2O_3–25 and Mn-Fe_2O_3–700 samples were degassed at 200 °C before measurement. Barrett-Joyner-Halenda (BJH) method was utilized to analyze the distribution of mesopores and micropores. The Fourier-transform infrared spectroscopy (FTIR, Nicolet iS50, Thermo) measurement of Mn-Fe_2O_3–25 and Mn-Fe_2O_3–700 samples was performed to identify surface functional groups. The catalyst morphology and elemental mapping of Mn-Fe_2O_3 were examined by field emission scanning electron microscopy (FE-SEM, SUS8230, Hitachi) and transmission electron microscopy (TEM, FEI-TALOS-F200X, Thermo). The leaching elements Fe and Mn were determined by inductive couple plasma optical emission spectrometry (ICP-OES, 5110, Agilent) with the following parameters: RF Power:1.20 KW; Plsama flow:12.0 L·min^{-1}; Auxiliary flow:1.00 L·min^{-1}. All samples were filtered twice by a 0.22 μM nylon filter prior to analysis. X-ray photoelectron spectroscopy (XPS, ESCALAB 250XI, Thermo) was conducted to investigate the valence state of elements using an Al K Alpha source in CAE mode at a pass energy of 30.00 ev and energy step size of 0.10 ev.

2.4. Extended X-ray absorption fine structure (EXAFS) measurement

The Fe and Mn K-edge X-ray absorption fine structure (XAFS) spectra were collected at the beamline of 4B9A in the Shanghai Synchrotron Radiation Facility (SSRF, Shanghai, operated at 3 GeV with a maximum current of 500 mA).

2.5. EXAFS data analysis

The Fe and Mn K-edge X-ray absorption fine structure (XAFS) spectra were collected at the beamline 4B9A in the Shanghai Synchrotron Radiation Facility. The EXAFS data were normalized and simulated using the ATHENA and ARTEMIS packages of IFEFFIT software. The global amplitude EXAFS (CN, R, σ^2, and ΔE_0) were obtained by nonlinear fitting, with least-squares refinement, of the EXAFS equation to the Fourier-transformed data in R-space, using Artemis software, EXAFS of the Fe and Mn foil is fitted and the obtained amplitude reduction factor S02 value was set in the EXAFS analysis to determine the coordination numbers (CNs) in the scattering path in sample. The obtained XAFS data was processed in Athena (version 0.9.26) [21] for background, pre-edge line and post-edge line calibrations. Then Fourier transformed fitting was carried out in Artemis (version 0.9.26). The k^3 weighting, k-range of 3–11.5 $Å^{-1}$ and R range of 1–3 Å were used for the fitting of MnO and Mn-Sample.

2.6. Catalytic measurement for SMX degradation

The SMX degradation experiment was conducted in a 100 mL conical flask. The initial pH of the reaction solution was adjusted to 9.20 using 1 mM borate buffer solutions at 25 °C. The reaction setup was placed on a DF-101S heat-collecting constant temperature heating magnetic stirrer and stirred at 500 rpm. At predetermined intervals, samples were withdrawn, immediately quenched, and filtered through 0.22 μm organic membranes before being transferred to vials for analysis. Each experiment was performed in triplicate, and results are presented as mean values with standard deviations in the figures.

2.7. Density functional theory (DFT) calculation

The first-principles calculations are performed using the framework

of DFT within the Vienna Ab-initio simulation package (VASP). The exchange-correlation interaction was processed using a generalized gradient approximation (GGA) in the form of Perdew-Burke-Ernzerhof (PBE). The kinetic energy cutoff of the plane wave to extend the Kohn-Sham electron wave function was set to 450 eV. The iterative convergence of energy is 10^{-5} eV. All atoms were allowed to relax until the Hellmann-Feynman force was less than 0.01 eV·Å^{-1}. The Brillouin zone was sampled by a 1×2×1 k-point grid for $MnFe_2O_4$ and Vo-$MnFe_2O_4$. The charge density difference is used to study charge transfer, defined as Δρ=ρ(A/B)-ρA-ρB. Where Δρ is the charge density difference, ρ(A/B) is the total electron density of the model. ρA and ρB are the total electron densities of the isolated Fe site and the rest of the part, respectively.

A model was constructed to study the formation of oxygen vacancy and the reaction pathway of Fenton-like reaction. For Vo-$MnFe_2O_4$-Fe^{IV}=O hetero-structures, the atomic positions and lattice parameters of Vo on $MnFe_2O_4$ (110) were optimized. The reciprocal space was sampled by the Γ-centered Monkhorst-Pack scheme with a grid of 1×2×1. The optimized lattice parameters were as follows: a=16.14 Å, b=11.08 Å, c=24.72 Å, =β = =90 °. To facilitate computation, oxygen atoms was removed the from the (110) plane of $MnFe_2O_4$. The bond lengths of the Fe—O bonds before and after the adsorption of hydrogen peroxide were compared. The energy differences before and after the formation of ≡Fe^{IV}=O and electronic bond and anti-bond orbitals were utilized to contrast the formation tendency of the heterogeneous ≡Fe^{IV}=O at the Fe sites adjacent to the oxygen atom defects.

Gaussian16 was used to calculate the structure optimization and vibration frequency of all organic compounds under B3LYP/6-31G(d,p) functional and basis with SCRF=(SMD, solvent=water) and em=gd3bj dispersion correction [22]. Highest occupied molecular orbital (HOMO) and lowest unoccupied molecular orbital (LUMO) as well as the Energy gap were calculated and plotted using Multiwfn (3.7 Version) [23,24] and VMD (1.9.3 Version) [25].

3. Results and discussion

3.1. Characterization of catalysts

The XRD patterns of the Mn-doped Fe_2O_3 under different calcination degree are shown in Fig. 1a. The Manganese oxide was found as δ-MnO_2

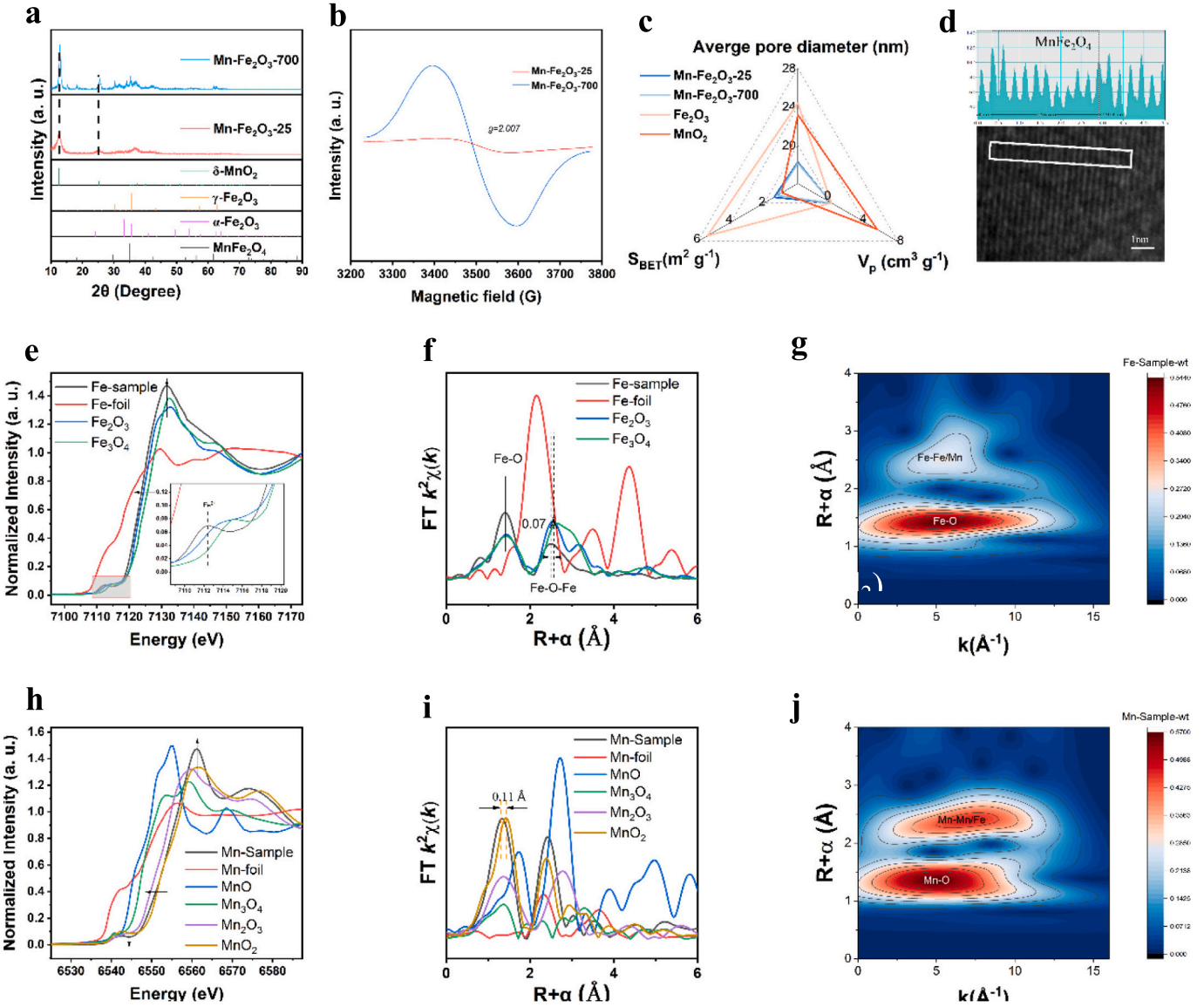

Fig. 1. Catalyst characterization: a XRD. b EPR. c BET parameter of Mn-Fe_2O_3. d TEM images and the profile plot of atomic column intensity variation of $MnFe_2O_4$. XANES spectrum of e Fe K-edge and h Mn K-edge in Mn-Fe_2O_3. FT $k^2\chi(k)$-weighted EXAFS signal of f Fe and i Mn in Mn-Fe_2O_3. WT for the k^2-weighted signal of g Fe and j Mn in Mn-Fe_2O_3.

(JCPDS 80–1098), which is easy to cause oxygen vacancy (Vo) than other MnO_2 configurations [26]. Another metal oxide is $MnFe_2O_4$ (JCPDS 10–0319) [27,28] , which is readily available in co-precipitation [29]. Ferrate oxide is also found as α-Fe_2O_3 (JCPDS 33–0664) [30]. The lattice planes (001) and (002) belonging to MnO_2 shifted obviously with the addition of the calcination process due to the compressive distortion of the cell caused by the defect of lattice structure [31]. The signal of EPR corresponding to Vo was enhanced with the addition of the calcination process in Fig. 1b and Fig. S1. The adsorption property of the catalyst is weak in Fig.1c. The microstructure and element distribution of the catalyst are confirmed by SEM and EDS mapping (Fig. S2, S3) and TEM (Fig.1d). The average particle size of the catalyst is about 1149 nm. There are some rough spherical or short rod-like and spherical structures (20–1000 nm) attributed to Fe and Mn oxidase [27]. (311) lattice plane belonging to $MnFe_2O_4$ was observed in Fig. 1d and Fig. S3 c_2.

In Fig.S4, the chemical bonds belonging to Fe—O and Mn—O are weakened in the functional group region and amplified in the fingerprint region. According to the Noda rule, Fe—O in the material weakens and then strengthens before Mn—O (Fig. S4, Fig. S5 and Text S7). To further detect inner structure information of the atom, the remarkable red shift (7124.42 → 7123.67 eV) Fe K-edge X-ray adsorption near-edge structure (XANES) shows that the iron in Mn-Fe_2O_3 exhibits a lower valence state and a higher electron density (Fig. 1e) [16]. The Fe K-edge pre-edge region in the partial enlarged figure is attributed to the dipole-forbidden 1 s → 3d [32], which usually indicates the appearance of a less symmetrical tetrahedral site of the metal (γ-Fe_2O_3) [33]. The enhancement of the white line peak means that it is easier for the electrons of the Fe sample to make the 1 s → 4p orbital transition, which involves the oxygen deficient [33]. Fig. 1f shows the X variation of the Fourier transforms (FT) of the $k^2\chi(k)$-weighted extended XAFS (EXAFS), exhibited a prominent peak at 1.92 Å which were corresponding to the

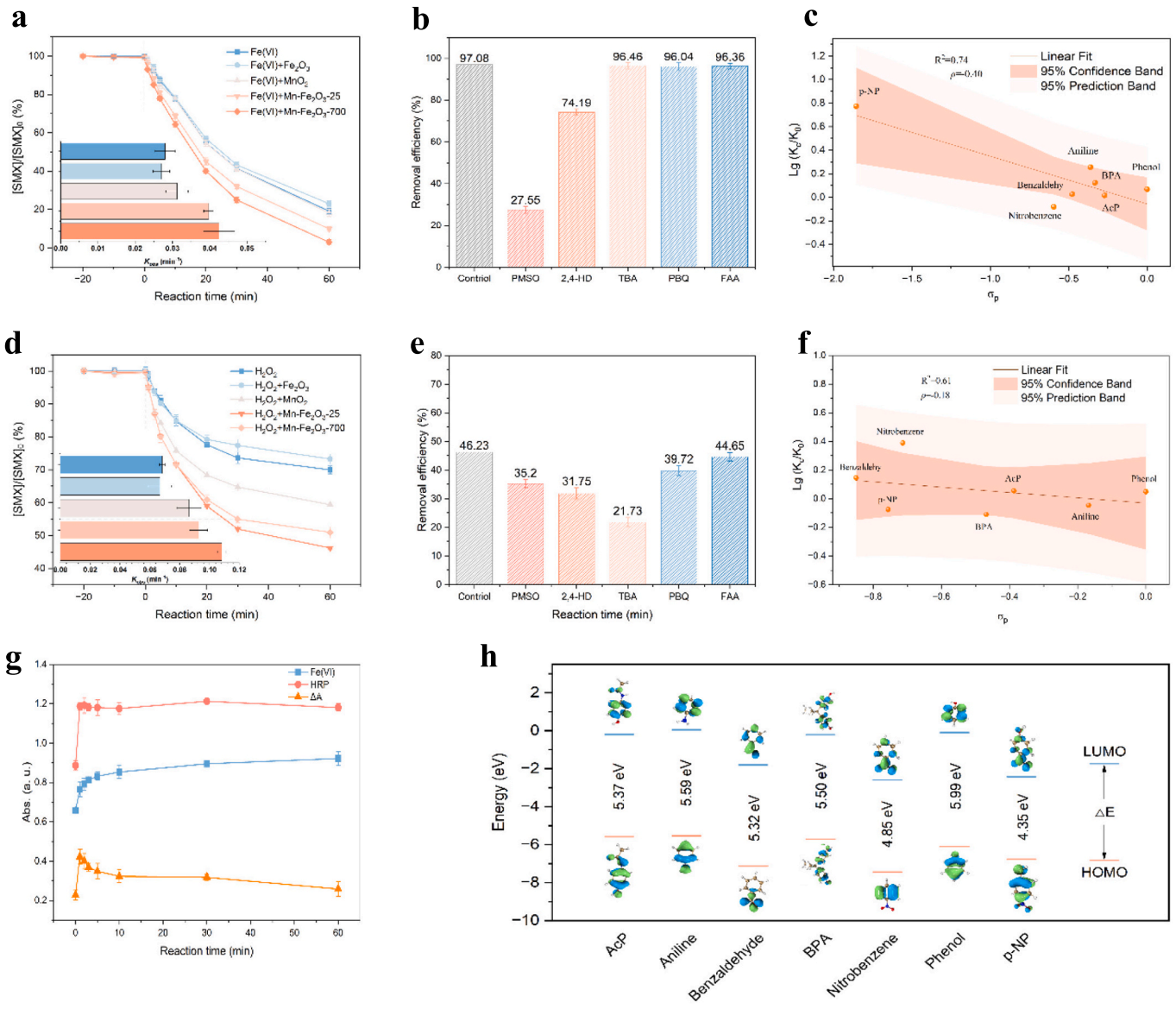

Fig. 2. Sulfamethoxazole (SMX) degradation and corresponding K_{obs} in a Fe(VI) system (Experimental conditions: [Fe(VI)] = 200 μM, [SMX] = 10 μM, catalyst = 0.2 g·L^{-1}, pH = 9.20, 1 mM borate buffer) and d H_2O_2 system (Experimental conditions: [H_2O_2] = 50 mM, [SMX] = 10 μM, catalyst = 0.2 g·L^{-1}, pH = 6.87 at 25 °C). Effect of quenching experiment on SMX degradation in b Fe ，(VI) system and e H_2O_2 system (each quenching agent applied at a 100-fold molar excess relative to Fe (VI) or H_2O_2). Correlation analysis between the Hammett constants of the selected phenolics and the ratios of the removal rate in c Fe(VI) system and f H_2O_2 system. g Different H_2O_2 production in different time gaps after horseradish Peroxidase (HRP) catalyzation. h Energy gap between HOMO and LUMO of selected phenolic compounds.

Fe—O band distances in tetrahedron sites (Table S1). The 2nd peak corresponding to the 2nd coordination shell (2.89 Å), which is corresponding to Fe—Fe distances [34]. The faster decay of the R-space of the Fe element means severe structural disorder [35]。 Wavelet transform (WT) analysis of EXAFS (Fig. 1g and Fig. S6) reveals that the Fe—O bond in the catalyst is moving slightly into higher K-space, possibly as a result of the overhanging Fe—O bond that dominates the material surface [36], compared with Fe_2O_3 and Fe_3O_4 in standard samples (Fig. S7). The pre-edge of Mn reveals that there is more symmetrical octahedral coordination around Mn (Fig. 1h) [37] , which means that the hybridization of the d orbitals of Mn with the P orbitals of the ligand O is weaker and the probability of electron transition is lower [38]. It is worth noting that the coordination number of Mn—O is also less than 6 (Table S2), which may be caused by the appearance of oxygen vacancies [36]. The white line peak of Mn also increased. Interestingly, compared with MnO_2 crystal, the first coordination shell of the sample Mn has a 0.11 A reduction corresponding to the Mn—O bond, which may be due to the increase of Mn in tetrahedral coordination and the decrease of Mn in octahedral coordination. The WT of Mn shows that the height (coordination number) of Mn-Mn/Fe is between MnO_2 and Mn_2O_3 (Fig. 1j, Fig. S8 and Fig. S9).

3.2. Catalytic performance

Because the oxidation capacity of Fe(VI) is highly pH-dependent [39] and strong complexation between phosphate anions and Fe(V) species [40], borate buffer solution (BBS) was selected for Fe(VI) system. Considering the low specific surface area and adsorption capacity of the catalyst (Table S3), the adsorption of organic matter was initially neglected.

In the Fe(VI) system, the Mn-Fe_2O_3–700 achieved a degradation efficiency of 97.54 % for SMX within 60 min, compared with 80.87 % for Fe(VI) alone (Fig. 2a). The difference became even more pronounced in the H_2O_2 system, where SMX degradation decreased from 70.21 % (with Mn–Fe_2O_3–700) to 46.23 % (H_2O_2 alone), as shown in Fig. 2d. The K_{obs} of SMX degradation by H_2O_2 increased from 0.6861 (H_2O_2 alone) to 0.9267 (H_2O_2 with Mn-Fe_2O_3–700). The activation effect of the catalyst on the Fe (VI) and H_2O_2 systems was further verified in Fig. S10 and Table S4. In addition, the interference experiments indicated that both Cl^- and HA exhibit inhibitory effects on the oxidation system (Fig.S11 and S12). In the H_2O_2 system, HCO_3^- exhibits an inhibitory effect because HCO_3^- quenches a portion of ·OH, while in the Fe (VI) system, the increase of HCO_3^- will reduce the pH of the solution and further enhance the oxidizing property of Fe (VI). Evaluation of the degradation intermediates from the two systems (Fig. S13 and S14) revealed that the intermediates generated in the H_2O_2 system exhibit higher toxicity than those in the Fe(VI) system. This is partly because Fe(VI) achieves more thorough mineralization of SMX, and partly due to the non-selective attack characteristic of free radicals—these radicals tend to cleave key structures in the SMX molecule such as N-S bonds and benzene ring side chains, leading to the formation of intermediates with highly toxic functional groups including nitro (-NO_2) and aldehyde (-CHO) groups. Although MnO_2 is known to catalyze H_2O_2 decomposition, its catalytic effect didn't appear apparently in Fe(VI) system in Fig. 2a [7].The catalytic performance of the as-prepared catalyst toward H_2O_2 activation was benchmarked against that of other reported catalysts (Fig. S15). While the H_2O_2 activation efficiency of this catalyst is moderate relative to existing counterparts, it stands out for its remarkably low dosage requirement—a key practical advantage for scalable applications.

Quenching experiments revealed that hypervalent iron species and R• radicals dominate SMX degradation in the Fe (VI) system (Fig. 2b), while ·OH, R•, $O_2^{\bullet -}$ and Fe^{IV}=O were all contributors in H_2O_2 system (Fig. 2e and Fig. S16). The catalyst showed poor reusability in the Fe(VI) system, with a sharp decline in performance during the second cycle (Fig. S15), whereas its activity was well maintained in the H_2O_2 system. This is because in the Fe(VI) system, Fe(VI) converts into Fe_2O_3 and Fe $(OH)_3$, and the catalyst is severely contaminated by the oxidation products (Fig. S18). XPS results (Fig. S19 and S20) show that after the reaction in the H_2O_2 system, the Fe 2*p* peak shifts toward the region of lower binding energy, indicating that Fe is gaining electrons; in contrast, the Mn 2*p* peak shifts toward the region of higher binding energy, which means Mn is losing electrons. In other words, H_2O_2 promotes the conversion of Mn to a higher oxidation state, while Fe transforms to a lower oxidation state. In the Fe(VI) system, although Mn shows a greater transition from low to high oxidation states, the conversion of Fe^{3+} to Fe^{2+} is relatively limited. This is mainly caused by the interference of exogenous Fe(VI). Interestingly, H_2O_2 was produced in the Fe(VI) system (Fig. 2g and Fig. S21), although it is hard for H_2O_2 to be catalyzed in the Fe(VI) solution. This phenomenon can be explained by two factors. First, excess H_2O_2 reacts with hydroxyl radicals to inhibit the degradation of organic matter [41,42](Eqs.(1), (2)).

$$HO\cdot + H_2O_2 \rightarrow HOO\cdot + H_2O \; K = 2.7 \times 10^7 \; mol\cdot L^{-1}\cdot S^{-1} \quad (1)$$

$$HO\cdot + HOO\cdot \rightarrow HO + O_2 \; K = 6.0 \times 10^9 \; mol\cdot L^{-1}\cdot S^{-1} \quad (2)$$

The species-specific rate constants were determined by a nonlinear least-squares regression in the tested pH range 7–12, the overall reaction is mainly controlled by the following two reactions 3 and 4 [39], whereas H_2O_2 is not stably present under these conditions. The quench reaction rate of TBA with hydroxyl radical is only $5 \times 10^8 \; M^{-1} \; s^{-1}$ [43]. Once single electron transfer processes (ETPs) occur in the H_2O_2 system, the inhibitory effect on organic matter degradation is further intensified (Eqs.(5)) [44], so that excess H_2O_2 does not show the better removal efficiency.

$$HFe^{VI}O_4^- + HO_2^- \rightarrow \text{products} \; K = 1.34 \pm 0.2 \times 10^6 \; M^{-1}\cdot s^{-1} \quad (3)$$

$$Fe^{VI}O_4^{2-} + HO_2^- \rightarrow \text{products} \; K = 2.32 \pm 0.2 \times 10^2 \; M^{-1}\cdot s^{-1} \quad (4)$$

$$e_{aq}^- + H_2O_2 \rightarrow HO\cdot + OH^- \; K = 1.6 \times 10^{10} \; M^{-1}\cdot s^{-1} \quad (5)$$

Second, H_2O_2 undergoes inefficient decomposition under alkaline conditions, which limits its participation in the reaction [45]. Also, it is well established that the self-decomposition of Fe (VI) significantly increases the pH of the solution.

The slope of Linear free energy spectrum (ρ) can reflect the characteristics of substituents in the aromatic ring. When $\rho<0$, the electron donor groups are conducive to the reaction, indicating that the rate control is the process of the accumulation of positive charge in the reaction center [7,46,47], which is more remarkable in Fe(VI) systems (Fig.2c, 2f, Fig. S22, S23 and Table S5-S8). The more negative value of σ_p in aromatic compounds than in Phenol further reflects their electron-donating properties in Fe(VI) systems (σ_p= −1.85 in Fe(VI) system and −0.76 in H_2O_2 system), even though the -NO2 functional group of p-NP in para-substituents exhibits electron-withdrawing properties in conventional organic reactions (σ_p= +0.778) [48]. Energy gap (ΔE=| EHOMO-ELUMO|) was further verified the nature affected by electrophilic attack activity in the aromatic compound (Fig. 2h). Whatever in Fe(VI) system or in H_2O_2 system, p-NP is possess of lower EHOMO and Energy gap, indicating that higher reactivity toward oxidation. Similar properties were found in Nitrobenzene and benzaldehyde. Overall, the combination of Linear free energy spectrum and energy gap further elucidates the distinct oxidation nature of Fe(VI) and H_2O_2 on aromatic compounds and compared the influence of benzene ring substituents on oxidation performance.

3.3. Detector for hypervalent ferrate-oxo

In addition to free radicals, Fe^{IV}=O species also accelerate the oxidation of SMX. The transformation of Fe^{3+} to Fe^{2+} in H_2O_2 solution was confirmed via by the 2,2'-Bipyridyl colorimetric reaction [49]. In this tyipcal Fenton process, the addition of catalyst enhanced the

transformation of PMSO to $PMSO_2$ (Fig. 3a). As a homogeneous species of hypervalent iron-oxo, $[(H_2O)_5Fe^{IV}=O]^{2+}$ with a terminal oxo moiety can be generated in this system [50]. With the discovery of heterogeneous hypervalent iron[$\equiv Fe^{IV}=O$] [17,51], the various $Fe^{IV}=O$ species in the H_2O_2 system require further identification.

The formation of a catalyst-H_2O_2 complex can increase the potential on the catalyst surface, which is similar to applying a potential directly to the catalyst acting as an anode [18]. Therefore, the peak potential of 1.20 V and 1.09 V, corresponding to $Fe^{IV}=O$ and PMSO (Fig. 3b). However, these experiments primarily identify $Fe^{IV}=O$ in the liquid phase. Regarding the formation of the catalyst-H_2O_2 complex on the material surface, characteristic spectral signals were tentatively probed using diffuse reflectance ultraviolet-visible (DR-UV–Vis) spectroscopy. It is reflected by the spectra that the adsorption intensity in the 200–560 nm range is attenuated, and this broad absorption band exhibits spectral features like the previously reported $\equiv Fe^{IV}=O$ species, which have been observed in Fe-based zeolites and potassium-intercalated iron oxychloride systems [17,19]. Notely, the reactive iron species exhibited red-shifted peaks at 371 nm and 560 nm region by 5–21 nm, compared to non-heme iron enzymes [52]. In Fig. 3d and Fig. S24, $\equiv Fe^{IV}=O$ species was also observed in 844 cm^{-1} on catalyst surface, which is ubiquitous in H_2O_2 and PMS system with heterogeneous iron-based catalyst [53,54]. A band at 791 cm^{-1}, attributed to Fe–O–O, likely represents an intermediate in Fe=O evolution, as Fe–O–O–Fe linkages can form readily between adjacent Fe=O [55].

3.4. Evaluation of catalytic reactivity

ICP-OES analysis (Fig. 4a and b) revealed that metal leaching from the catalyst was enhanced in the presence of 1 mM H_2O_2. The leaching concentration of the metal on the surface of the material reached 0.185 $mg{\cdot}L^{-1}$ in 1 M H_2O_2 solution, while the leaching amount of Mn was 0.084 $mg{\cdot}L^{-1}$. When the H_2O_2 concentration was below 50 mM, the leaching amount of Fe ions decreased significantly (from 0.032 $mg{\cdot}L^{-1}$ to 0.002 $mg{\cdot}L^{-1}$) [47] , implying a notable reduction in the generation of homogeneous $Fe^{IV}=O$. Compared with Fe_2O_3, Mn-Fe_2O_3 exhibited less Fe leaching but higher Mn leaching than MnO_2. This is attributed to the relatively large ionic radius of Mn^{2+}, which weakens the bonding with surrounding oxygen ions in the octahedral spinel lattice. Therefore, more heterogeneous $\equiv Fe^{IV}=O$ is formed on the surface of the Mn-doped iron-based spinel catalyst, leading to the formation of $PMSO_2$ and the degradation of SMX. XPS analysis further indicated the Fe leaching of Fe predominantly originated from Fe^{3+}, whereas the Mn leaching was primarily from Mn^{2+}.

To verify the ETP during the activation of H_2O_2 and the oxidation of organic compounds on the catalyst electrode, galvanic oxidation process (GOP) experiment was conducted (Fig. 4c). After adding H_2O_2 to the glassy carbon electrode (GCE), the potential started to decrease and then

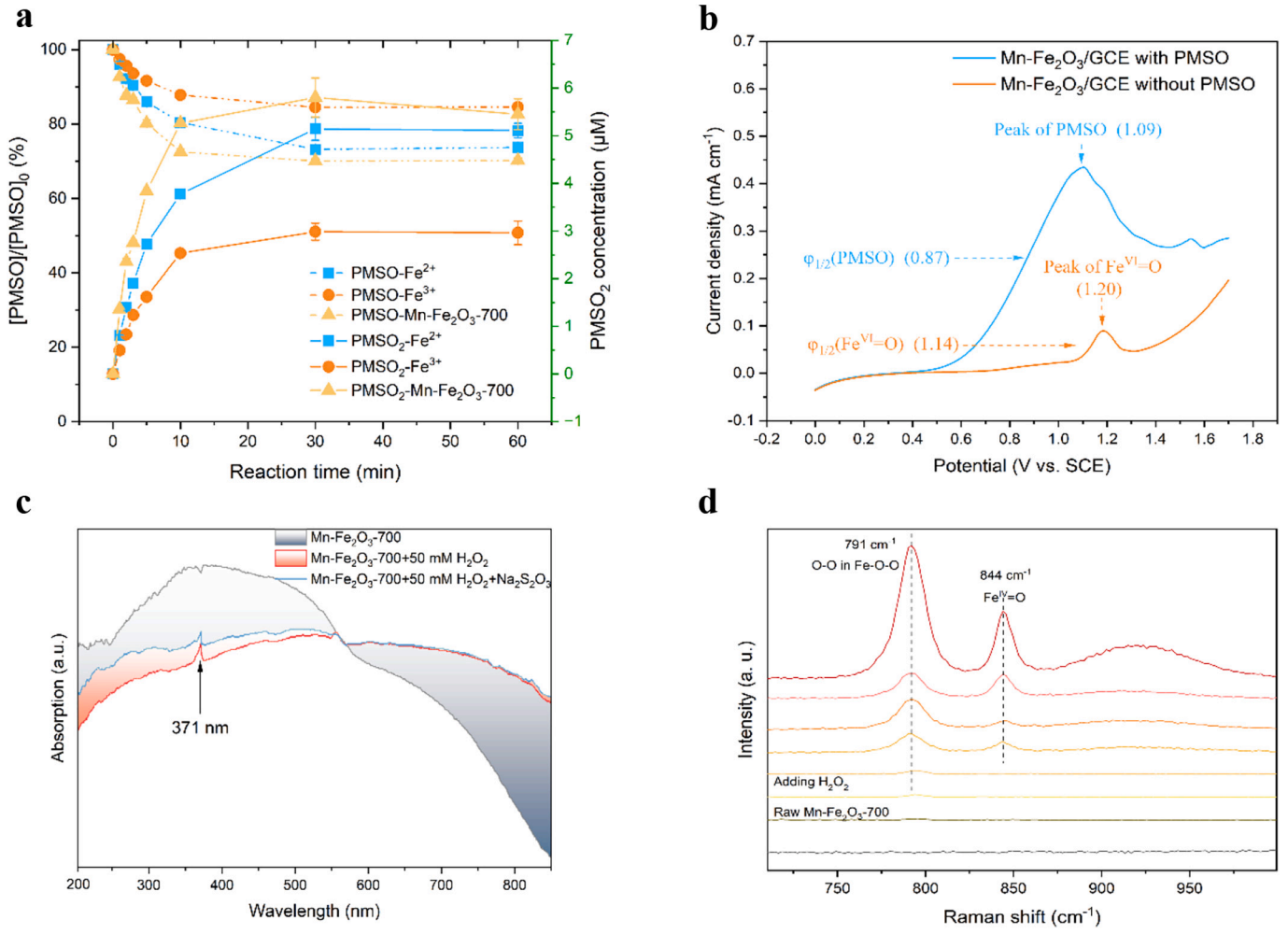

Fig. 3. **a** The transformation between PMSO and $PMSO_2$ in Mn-Fe_2O_3/H_2O_2 system (Experimental conditions: [PMSO] = 20 μM, [H_2O_2] = 50 mM, catalysts = 0.2 $g{\cdot}L^{-1}$). **b** LSV measurements on Mn-Fe_2O_3/GCE for Fe^{IV}=O detection (Experimental conditions: [Na_2SO_4] = 50 mM, scan rate 10 $mV{\cdot}S^{-1}$, pH = 7.0 at 25 °C). **c** Experimental DR-UV–Vis spectra of Mn-Fe_2O_3–700 before and after reaction with H_2O_2. **d** Raman spectra of Mn-Fe_2O_3–700 reacted with 50 mM H_2O_2 (λ_{ex} = 532 nm).

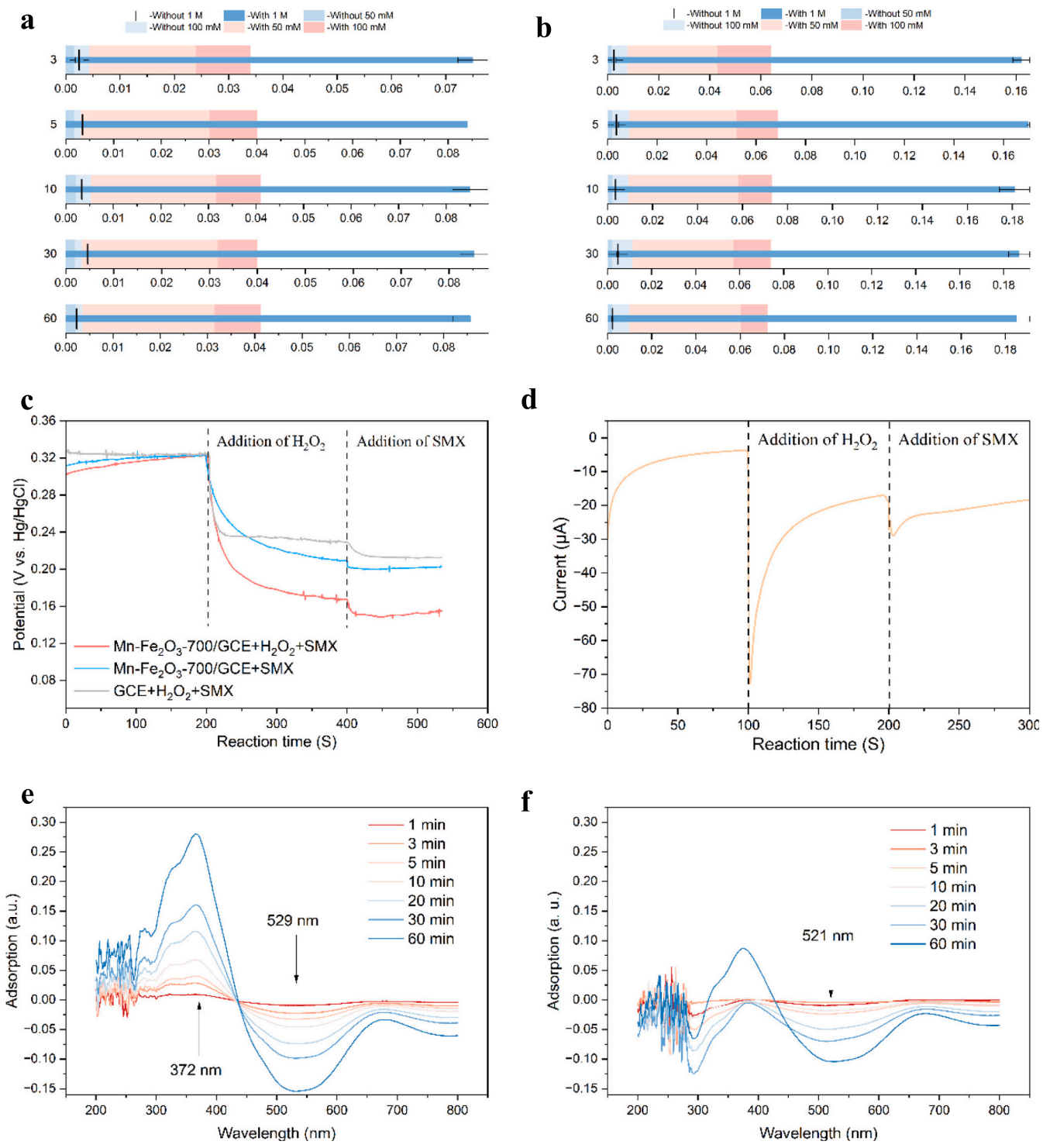

Fig. 4. Inductively coupled plasma-optical emission spectrometry (ICP-OES) detection for **a** Fe and **b** Mn (Experimental condition: [Catalyst] = 0.2 g·L^{-1}, pH = 6.87). **c** Open-circuit potential (OCP) and **d** current detect. UV–Vis differential analysis spectrum for ion concentration detection in Fe (VI) system with **e** 0.1 g·L^{-1} and **f** 0.2 g·L^{-1} catalyst (Experimental condition: [Fe(VI)] = 200 μM borate buffer (100 mM, and pH = 9.2) at 25 °C).

gradually reached equilibrium at (+0.23 V). Due to the fact that the equilibrium potential is lower than the oxidation potential of SMX, the potential gradually decreased to +0.21 V with the following addition of SMX [56]. When adding H_2O_2 to the Mn-Fe_2O_3–700/GCE, a reaction occurred between the H_2O_2 and the catalyst, resulting in a potential decrease to +0.15 V. As chronoamperometry measurements shown in Fig. 4d, the injection of H_2O_2 caused large current decrease, revealing the direction of electron transfer from the organic compounds to the H_2O_2 activated by the catalyst (Fig. 4d) [57]. The GOP results confirm Mn–Fe_2O_3–700 acts as an efficient electron mediator, enabling interfacial electron transfer and effective SMX oxidation [58]. Unlike H_2O_2, when GCE is loaded onto the catalyst, the addition of Fe(VI) causes a sharp drop in potential followed by a significant increase, and ultimately reaches the highest potential (Fig. S25). This indicates that the oxidant (Fe(VI)) in the system is rapidly consumed and has a fast electron transfer rate, demonstrating the strongest catalytic oxidation activity.

The It curve indicates that after the addition of Fe(VI), the current gradually decreases from the peak, suggesting that the concentration of Fe(VI) in the system decreases with the reaction. When SMX is added at approximately 200 s, the current briefly drops (or changes) again, and then enters a new slow attenuation stage. The amplitude of the current change reflects that the reaction kinetics is obvious and efficient. This enhanced performance is attributed to the lower electrochemical impedance and faster chemical reaction rate of the calcined catalyst (Fig. S26 and S27), facilitating rapid electron migration from the bulk material to its surface [59,60].

Illumination of hypervalent iron was monitored by UV–Vis spectroscopy [61,62], and showed isosbestic conversion with bands at 245, 372 and 532 nm in BBS(Fig. S28). In the presence of the catalyst (Fig. 4e, f and Fig. S29), the absorbance of the hypervalent iron species increased from −0.15 at 529 nm to −0.10 at 521 nm. In contrast, the absorbance of the single hypervalent iron species in the BBS buffer solution decreased to −0.48 at 532 nm after 60 min (Fig. S29). This pattern is similar to the decrease in absorbance at 550 nm caused by N4Py in the H_2O_2 system [63], indicating that the addition of the catalyst slows down the decay of the hypervalent iron species in the Fe(VI) system. The absorbance at 372 nm also increased due to the formation of Fe(IV) as shown in Fig. 4e and Fig. S29 [12]. However, when the catalyst concentration was further increased, the absorption band in 372 nm at this position became significantly attenuated, likely due to scattering and interference from particulate matter.

The effect of catalyst addition on Fe(VI) attenuation was further examined. As shown in Fig. S30 and Fig. S31, the attenuation trend of the UV–Vis spectrum was extremely close to that of Fig. S28 and Fig. S29. At a concentration of 50 μM Fe (VI), the self-decay rate of Fe (VI) decreased with the addition of the catalyst. After 60 min, the absorbance decay at 524 nm decreased from −0.347 a.u. (0.1 $g{\cdot}L^{-1}$ of catalyst) to −0.279 a.u. (0.2 $g{\cdot}L^{-1}$ of catalyst) and −0.234 a.u. (0.3 $g{\cdot}L^{-1}$ of catalyst), compared to −0.244 a.u. without catalyst addition. Since Fe (VI) is also consumed by $ABTS^{\bullet+}$ [64],its decay was further evaluated by detecting the attenuation of ABTS. As depicted in Fig. S32, the absorbance of $ABTS^{\cdot+}$ decreased from an initial value of approximately 1.119 a.u. to 0.504 a.u. without the catalyst. Conversely, when the catalyst loadings were 0.1 $g{\cdot}L^{-1}$, 0.2 $g{\cdot}L^{-1}$, and 0.3 $g{\cdot}L^{-1}$, the corresponding absorbances of $ABTS^{\cdot+}$ after 60 min were 0.276 a.u., 0.424 a.u., and 0.497 a.u., respectively, indicating that the catalyst effectively suppressed Fe(VI) decay.

Notably, the Mn-Fe_2O_3-700 catalyst exhibited a biphasic effect on the decay of Fe(VI). Initially, it accelerated the decomposition of Fe(VI); however, after 15 min, the decay rate significantly decreased. This phenomenon can be attributed to the rapid reaction between the catalyst and H_2O_2 generated in the later stages of the reaction, which suppresses direct reaction between H_2O_2 and Fe(VI). Additionally, the formation of $\equiv Fe^{IV}{=}O$ species through the interaction between H_2O_2 and the catalyst is another crucial factor contributing to the observed decrease in $ABTS^{+}$ concentration. A correlation analysis between the adsorption spectra of $ABTS^{\cdot+}$ and UV–Vis measurements was conducted. As shown in Fig. S33, the decay of Fe(VI) determined by the ABTS method was in good agreement with that measured by UV–Vis spectroscopy. Without catalyst, the difference values obtained from ABTS and UV–Vis measurements showed excellent consistency. Although the addition of the catalyst initially increased and then decreased the ABTS decay, the overall correlation remained significant. Excessive catalyst, however, not only interfered with UV–Vis measurements but also increases material costs, highlighting the importance of optimizing catalyst dosage.

3.5. Mechanisms of defects-induced $\equiv Fe^{IV}{=}O$ generation

The heterogeneous generation pathway about $\equiv Fe^{IV}{=}O$ in iron complex activated H_2O_2 system is widely recognized [13,19]. In this study, it was found that defects-induced $Fe^{IV}{=}O$ generation pathway in Vo-$MnFe_2O_4$ occurs more readily. DFT calculations show that during the adsorption process of Fe and H_2O_2, the Fe—O bond length shortens from 2.22 Å in $MnFe_2O_4$ to 2.00 Å in Vo-$MnFe_2O_4$ (Fig. 5a and Fig. S34). The major rate-limiting step of this reaction lies in the formation of H-OOH (transition state) after the adsorption of H_2O_2, with a free-energy barrier of 2.08 eV, because the bond energy of H-OOH is much greater than that of the O—O bond. In the Vo-$MnFe_2O_4$ material, the free-energy barrier of this step is only 0.99 eV (Table S9). Subsequently, the O—O bond in the *OOH moiety cleaves, and ultimately yielding the $Fe^{IV}{=}O$ species. The crystal orbital Hamilton populations (COHP) analysis (Fig. 5b) verifies that $\equiv Fe^{IV}{=}O$ on Vo-$MnFe_2O_4$ is more stable than Fe-*OOH, especially when the spin of iron is equal to 2 (Table S10 and S11). Projected COHP (pCOHP) results reveal that the Fe d_{yz}-O bond exhibits the highest -pCOHP value (0.641) among all Fe 3d orbitals (Table S11), indicating that this bond dominates the electronic stabilization of the $Fe^{IV}{=}O$ species. Additionally, the -pCOHP value of 0.645 for Fe d_{yz}-O p_y bond highlights that Fe d_{yz}-O p_y is the dominant channel for d orbital electron transportation.

To gain deeper insight into the electronic structure of the Fe sites, density of states (DOS) analysis was performed. After introducing Vo, the energy levels within the range of −1.11 to 1.16 eV are mainly contributed by the hybrid states composed of the Fe 3*d* states. After the formation of $\equiv Fe^{IV}{=}O$, the hybrid Fe 3d states shift slightly, with the energy eigenvalues distributed within the range of −1.21 to 1.39 eV. The d-band center (DOWN) data in Fig. 5c indicates that due to the decrease in the occupation of the anti-bonding states after the formation of the $\equiv Fe^{IV}{=}O$ species, the overall structure of the catalyst becomes more stable, and the chemical bonding interactions between the transition metals and small molecules are strengthened [65]. Overall, the symmetry between the up-spin (α-spin) and down-spin (β-spin) electrons decreases, implying an increase in the spin electrons. Furthermore, after coordination with *O, by comparing the Projected DOS of the Fe-3d orbitals (Fig. S35), the significant increase in spin electrons mainly results from the extraction of the coordinated O atoms on the Fe-3dyz orbitals [66], leading to a higher Fe oxidation state and spin number.

Differential charge (Fig. 5d and e) and Bader charge (Table S12–14) analysis further reveal that Fe in Vo-$MnFe_2O_4$ near the Vo gains 0.45 more electrons compared to that in $MnFe_2O_4$. This electron enrichment of Fe facilitates subsequent electron transfer to the coordinating O atoms. After the formation of $\equiv Fe^{IV}{=}O$, Fe atom donates 0.65 electrons to O atom, highlighting its role as the electron donor in the Fe—O bond formation process. From the perspective of frontier molecular orbital theory (Fig. 5f), the $\equiv Fe^{IV}{=}O$ species in its $S{=}2$ spin state exhibits strong π and σ bonding interactions between Fe and O. These bond interactions promote substantial charge donation from the oxygen group to the formal $\equiv Fe^{IV}{=}O$, stabilizing the high-valent iron-oxo species [11].

4. Conclusions

This study reveals that introducing oxygen vacancies into Mn–Fe_2O_3 fundamentally reshapes the electronic environment of surface Fe sites and redirects the reaction pathways of Fe (VI) and its self-generated H_2O_2. Spectroscopic evidence, together with DFT calculations, shows that Vo sites increase the electron density of adjacent Fe atoms and facilitate O-atom trapping during H_2O_2 adsorption. This promotes O—O bond activation and lowers the energy barrier for the formation of heterogeneous Fe(IV)=O, a species that plays a decisive role in oxygen-atom transfer reactions. The coexistence of Fe(VI) and Vo-rich Mn–Fe_2O_3 creates a coupled mechanism: Fe(VI) decomposition produces H_2O_2, while the defect-engineered catalyst selectively channels this H_2O_2 through a high-valent iron–oxo pathway rather than radical-driven decay. Electron-transfer measurements confirm that Vo enhances interfacial charge flow, enabling rapid cycling between Fe oxidation states and stabilizing reactive intermediates. The catalyst simultaneously slows Fe(VI) self-decay and accelerates pollutant oxidation, demonstrating that the modulation of surface defect chemistry can shift the dominant oxidative species from short-lived radicals to

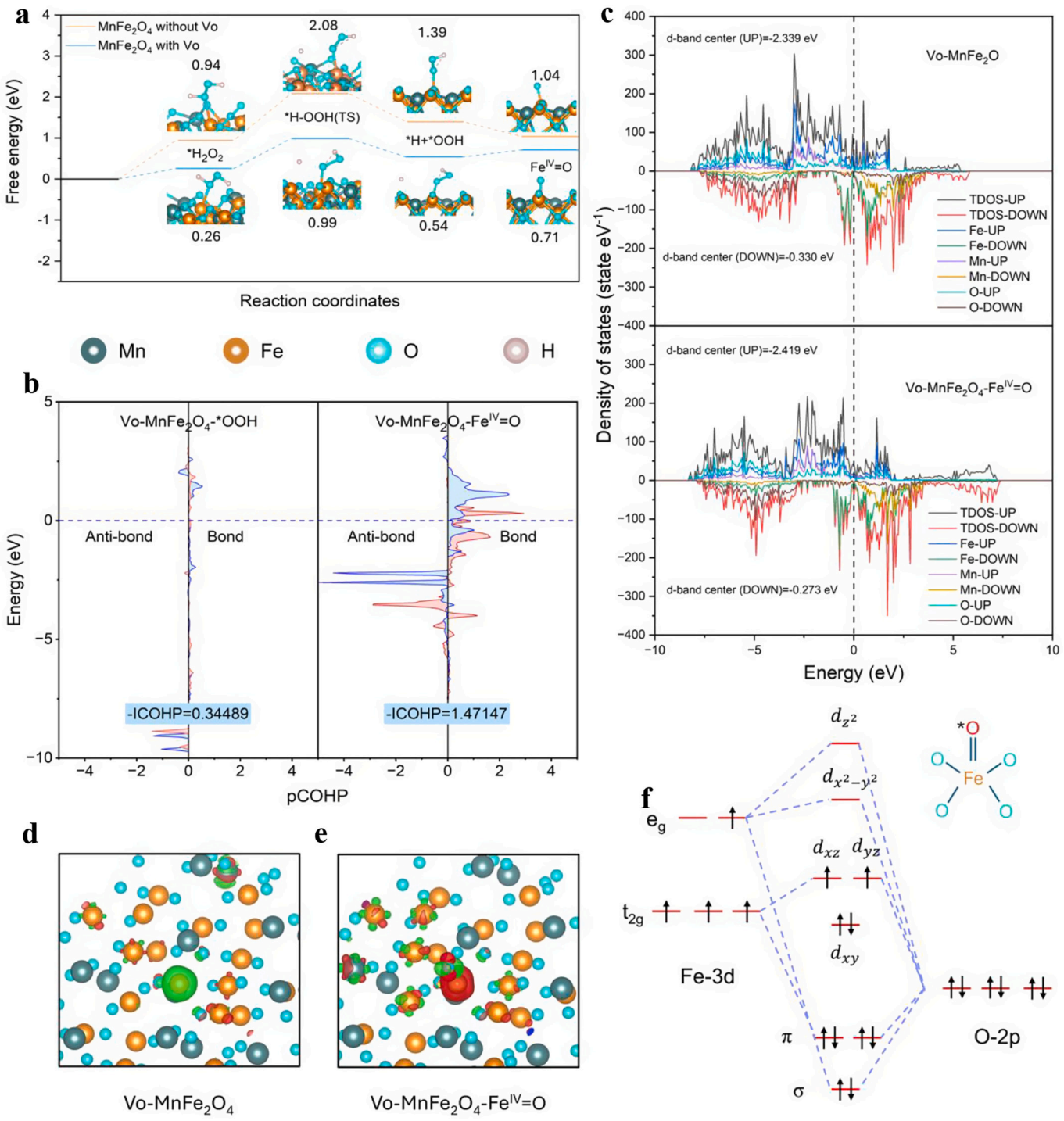

Fig. 5. **a** Reaction pathway and the energy profile diagram of $\equiv Fe^{IV}=O$ generation on $MnFe_2O_4$ and Vo-$MnFe_2O_4$. **b** Projected DOS of Fe 3*d*, Mn 3*d*, O 2*p* in $MnFe_2O_4$, E_f is at 0 eV. **c** Projected crystal orbital Hamilton populations (pCOHP) in Vo-$MnFe_2O_4$ after adsorption of *OOH and *O. Charge density (red and green represent the dissipation and aggregations of electrons, respectively) in **d** Vo-$MnFe_2O_4$ and **e** Vo-$MnFe_2O_4$-Fe^{IV}=O. **f** Schematic illustration of bonding and anti-binding orbitals between Vo-adjacent Fe atom and the O atom. (For interpretation of the references to colour in this figure legend, the reader is referred to the web version of this article.)

structurally anchored Fe(IV)=O. Overall, the mechanistic insights gained here clarify how lattice defects in iron-based oxides govern oxidant activation at the atomic scale.

CRediT authorship contribution statement

Zhengming He: Writing – review & editing, Writing – original draft, Methodology, Funding acquisition, Formal analysis, Data curation, Conceptualization. **Cong Li:** Visualization, Validation, Supervision, Project administration, Funding acquisition, Conceptualization. **Jingzhen Su:** Writing – review & editing, Resources, Formal analysis, Data curation. **Kai Zhang:** Software, Resources, Methodology, Data curation. **Jiaxue zhu:** Writing – review & editing, Resources, Methodology. **Jieming Yuan:** Writing – review & editing, Supervision, Investigation, Data curation.

Declaration of competing interest

The authors declare that they have no known competing financial interests or personal relationships that could have appeared to influence the work reported in this paper.

Acknowledgments

This work was sponsored by the National Natural Science Foundation of China (Project No. 52442006), the Guangxi Key Research and Development Program (Project No. 2025FN9610713) and the Science and Technology Commission of Shanghai Municipality (Project No. 24DZ2306400).

Data availability

Data will be made available on request.

References

[1] T. Kamachi, M. Miyanishi, K. Yoshizawa, DFT study on the pH dependence of the reactivity of ferrate(VI), ACS Symp. Ser. 1238 (2016) 473–487.
[2] L. Wu, L. Wang, Y.-L. Liu, X.-N. Zhao, J. Ma, VUV activated Fe(VI) by promoting the generation of intermediate valent Iron and hydroxyl radicals, Environ. Sci. Technol. 58 (2024) 20256–20266.
[3] M.B. Feng, C. Jinadatha, T.J. McDonald, V.K. Sharma, Accelerated oxidation of organic contaminants by ferrate(VI): the overlooked role of reducing additives, Environ. Sci. Technol. 52 (2018) 11319–11327.
[4] J. Shu, K.M. Wang, V.K. Sharma, X.P. Xu, N. Nesnas, H.Y. Wang, Efficient micropollutants degradation by ferrate(VI)-Ti/Zn LDH composite under visible light: activation of ferrate(VI) and self-formation of Fe (III)-LDH heterojunction, Chem. Eng. J. 456 (2023) 141127.
[5] J.Z. Wu, Y.M. Cai, M.Q. Zhang, J.Z. Zhou, X.J. Zhou, W.K. Shu, J. Zhang, X. Huang, G.R. Qian, Y. Deng, Enhancing oxidative capability of ferrate(VI) for oxidative destruction of phenol in water through intercalation of ferrate(VI) into layered double hydroxide, Appl. Clay Sci. 171 (2019) 48–56.
[6] Y. Jiang, J.E. Goodwill, J.E. Tobiason, D.A. Reckhow, Effect of different solutes, natural organic matter, and particulate Fe(III) on ferrate(VI) decomposition in aqueous solutions, Environ. Sci. Technol. 49 (2015) 2841–2848.
[7] M.F. Luo, H. Zhang, P. Zhou, Z.K. Xiong, B.K. Huang, J.L. Peng, R. Liu, W. Liu, B. Lai, Efficient activation of ferrate(VI) by colloid manganese dioxide: comprehensive elucidation of the surface-promoted mechanism, Water Res. 215 (2022) 118243.
[8] J.X. Li, X.Y. Zhang, Y.K. Sun, L.P. Liang, B.C. Pan, W.M. Zhang, X.H. Guan, Advances in sulfidation of zerovalent iron for water decontamination, Environ. Sci. Technol. 51 (2017) 13533–13544.
[9] M.F. Luo, H.Y. Zhou, P. Zhou, L.D. Lai, W. Liu, Z.M. Ao, G. Yao, H. Zhang, B. Lai, Insights into the role of *in-situ* and *ex-situ* hydrogen peroxide for enhanced ferrate (VI) towards oxidation of organic contaminants, Water Res. 203 (2021) 117548.
[10] H. Bataineh, O. Pestovsky, A. Bakac, Electron transfer reactivity of the aqueous Iron(IV)–oxo complex, Outer-Sphere vs Proton-Coupled Electron. Transfer, Inorg. Chem. 55 (2016) 6719–6724.
[11] E.I. Solomon, A. Decker, N. Lehnert, Non-heme iron enzymes: contrasts to heme catalysis, P Natl. Acad. Sci. USA 100 (2003) 3589–3594.
[12] J.B. Gordon, A.C. Vilbert, I.M. DiMucci, S.N. MacMillan, K.M. Lancaster, P. Moënne-Loccoz, D.P. Goldberg, Activation of dioxygen by a mononuclear nonheme Iron complex: sequential peroxo, oxo, and hydroxo intermediates, J. Am. Chem. Soc. 141 (2019) 17533–17547.
[13] Y.K. Zhao, C.Y. Deng, D.J. Tang, L.Y. Ding, Y.C. Zhang, H. Sheng, H.W. Ji, W. J. Song, W.H. Ma, C.C. Chen, J.C. Zhao, A-Fe_2O_3 as a versatile and efficient oxygen atom transfer catalyst in combination with H_2O as the oxygen source, Nat. Catal. 4 (2021) 684–691.
[14] C. Lai, F. Huang, G. Zeng, D. Huang, L. Qin, M. Cheng, C. Zhang, B. Li, H. Yi, S. Liu, L. Li, L. Chen, Fabrication of novel magnetic $MnFe_2O_3$/bio-char composite and heterogeneous photo-fenton degradation of tetracycline in near neutral pH, Chemosphere 224 (2019) 910–921.
[15] K.Z. Huang, H.C. Zhang, Direct Electron-transfer-based peroxymonosulfate activation by Iron-doped manganese oxide (δ-MnO_2) and the development of galvanic oxidation processes (GOPs), Environ. Sci. Technol. 53 (2019) 12610–12620.
[16] W.D. Zhong, C.F. Yang, J. Wu, W.L. Xu, R. Zhao, H. Xiang, K. Shen, Q. Zhang, X. K. Li, Oxygen vacancies induced by charge compensation tailoring Ni-doped Co_3O_4 nanoflakes for efficient hydrogen evolution, Chem. Eng. J. 436 (2022) 134813.
[17] B.E.R. Snyder, P. Vanelderen, M.L. Bols, S.D. Hallaert, L.H. Böttger, L. Ungur, K. Pierloot, R.A. Schoonheydt, B.F. Sels, E.I. Solomon, The active site of low-temperature methane hydroxylation in iron-containing zeolites, Nat 536 (2016) 317–321.
[18] C. Cheng, W. Ren, F. Miao, X.T. Chen, X.X. Chen, H. Zhang, Generation of Fe^{IV}=O and its contribution to fenton-like reactions on a single-atom Iron-N-C catalyst, Angew. Chem. Int. Edit. 62 (2023) 202218510.
[19] J. Wang, K.-P. Hou, Y. Wen, H. Liu, H. Wang, K. Chakarawet, M. Gong, X. Yang, Interlayer structure manipulation of Iron oxychloride by potassium cation intercalation to steer H_2O_2 activation pathway, J. Am. Chem. Soc. 144 (2022) 4294–4299.
[20] C. Li, X.Z. Li, N. Graham, A study of the preparation and reactivity of potassium ferrate, Chemosphere 61 (2005) 537–543.
[21] B. Ravel, M. Newville, ATHENA, ARTEMIS, HEPHAESTUS: data analysis for X-ray absorption spectroscopy using, J. Synchrotron Radiat. 12 (2005) 537–541.
[22] M.J. Frisch, G.W. Trucks, H.B. Schlegel, G.E. Scuseria, M.A. Robb, J.R. Cheeseman, G. Scalmani, V. Barone, G.A. Petersson, H. Nakatsuji, X. Li, M. Caricato, A. V. Marenich, J. Bloino, B.G. Janesko, R. Gomperts, B. Mennucci, H.P. Hratchian, J. V. Ortiz, D.J. Fox, Gaussian 16 Rev. C.01, Wallingford, CT, 2016.
[23] T. Lu, A comprehensive electron wavefunction analysis toolbox for chemists, Multiwfn, J. Chem. Phys. 161 (2024) 082503.
[24] T. Lu, F. Chen, Multiwfn: a multifunctional wavefunction analyzer, J. Comput. Chem. 33 (2012) 580–592.
[25] H. William, D. Andrew, S. Klaus, VMD: Visual molecular dynamics, J. Mol. Graph. 14 (1996) 33–38.
[26] W.H. Yang, Z.A. Su, Z.H. Xu, W.N. Yang, Y. Peng, J.H. Li, Comparative study of α-, β-, γ- and δ-MnO_2 on toluene oxidation: oxygen vacancies and reaction intermediates, Appl. Catal. B-Environ. 260 (2020) 118150.
[27] Z. Wang, C. Lai, L. Qin, Y. Fu, J. He, D. Huang, B. Li, M. Zhang, S. Liu, L. Li, W. Zhang, H. Yi, X. Liu, X. Zhou, ZIF-8-modified $MnFe_2O_4$ with high crystallinity and superior photo-fenton catalytic activity by Zn-O-Fe structure for TC degradation, Chem. Eng. J. 392 (2020) 124851.
[28] R. Jain, S. Gulati, Influence of Fe^{2+} substitution on FTIR and raman spectra of Mn ferrite nanoparticles, Vib. Spectrosc. 126 (2023) 103540.
[29] R. Asadi, H. Abdollahi, M. Gharabaghi, Z. Boroumand, Effective removal of Zn (II) ions from aqueous solution by the magnetic $MnFe_2O_4$ and $CoFe_2O_4$ spinel ferrite nanoparticles with focuses on synthesis, characterization, adsorption, and desorption, Adv. Powder Technol. 31 (2020) 1480–1489.
[30] M. Tadic, D. Trpkov, L. Kopanja, S. Vojnovic, M. Panjan, Hydrothermal synthesis of hematite (α-Fe_2O_3) nanoparticle forms: synthesis conditions, structure, particle shape analysis, cytotoxicity and magnetic properties, J. Alloys Compd. 792 (2019) 599–609.
[31] X. Chen, J. Li, S. Cai, J. Chen, H. Jia, Two-step pyrolytic engineering of carbon-doped Co_3O_4 with rich defects for efficient low-temperature CO oxidation, J. Mater. Chem. A 8 (2020) 6619–6630.
[32] X.P. Wang, S.B. Xi, P.R. Huang, Y.H. Du, H.Y. Zhong, Q. Wang, A. Borgna, Y. W. Zhang, Z.B. Wang, H. Wang, Z.G. Yu, W.S.V. Lee, J.M. Xue, Pivotal role of reversible NiO_6 geometric conversion in oxygen evolution, Nature 611 (2022) 702–708.
[33] M.C. Ribeiro, G. Jacobs, R. Pendyala, B.H. Davis, D.C. Cronauer, A.J. Kropf, C. L. Marshall, Fischer-Tropsch synthesis: Influence of Mn on the carburization rates and activities of Fe-based catalysts by TPR-EXAFS/XANES and catalyst testing, J. Phys. Chem. C 115 (2011) 4783–4792.
[34] N.G. Imam, M. AbouHasswa, G. Aquilanti, S.I. El Dek, N. Okasha, A.A.G. Al Shahawy, Influence of polyethylene glycol on the physical properties of $Co_{0.2}Fe_{2.8}O_4$ nanoparticles used as MRI contrast agent; synchrotron radiation Fe K-edge XAFS, J. Mater. Res. Technol. 15 (2021) 4130–4146.
[35] F.D. Liu, H. He, Y. Ding, C.B. Zhang, Effect of manganese substitution on the structure and activity of iron titanate catalyst for the selective catalytic reduction of NO with NH_3, Appl. Catal. B-Environ. 93 (2009) 194–204.
[36] S.H. Wang, Q. Jiang, S.H. Ju, C.S. Hsu, H.M. Chen, D. Zhang, F. Song, Identifying the geometric catalytic active sites of crystalline cobalt oxyhydroxides for oxygen evolution reaction, Nat. Commun. 13 (2022) 6650.
[37] T. Yamamoto, Assignment of pre-edge peaks in K-edge x-ray absorption spectra of 3d transition metal compounds: electric dipole or quadrupole? X-Ray Spectrom. 37 (2008) 572–584.
[38] J. Shen, X. Chen, X. Xu, J. Li, Z. Wang, Y. Wang, P. Lin, J. Sun, B. Huang, T. Zhao, Engineering *d-p* orbital hybridization in a single-atom-based solid-state electrolyte for lithium-metal batteries, Angew. Int. Ed. Chem. 64 (2024) 202419367.
[39] Y. Lee, R. Kissner, U. von Gunten, Reaction of ferrate(VI) with ABTS and self-decay of ferrate(VI): kinetics and mechanisms, Environ. Sci. Technol. 48 (2014) 5154–5162.
[40] Z.S. Huang, L. Wang, Y.L. Liu, J. Jiang, M. Xue, C.B. Xu, Y.F. Zhen, Y.C. Wang, J. Ma, Impact of phosphate on ferrate oxidation of organic compounds: an underestimated oxidant, Environ. Sci. Technol. 52 (2018) 13897–13907.
[41] N. Liu, Z.D. Lei, T. Wang, J.J. Wang, X.D. Zhang, G. Xu, L. Tang, Radiolysis of carbamazepine aqueous solution using electron beam irradiation combining with hydrogen peroxide: efficiency and mechanism, Chem. Eng. J. 295 (2016) 484–493.
[42] J.K. Im, I.H. Cho, S.K. Kim, K.D. Zoh, Optimization of carbamazepine removal in O_3/UV/H_2O_2 system using a response surface methodology with central composite design, Desalination 285 (2012) 306–314.
[43] S. Garg, Y.T. Yuan, M. Mortazavi, T.D. Waite, Caveats in the Use of Tertiary Butyl Alcohol as a Probe for Hydroxyl Radical Involvement in Conventional Ozonation and Catalytic Ozonation Processes, ACS ES&T Eng 2 (2022) 1665–1676.
[44] F. Cheng, J.L. Wang, Regulating hydroxyl radicals (•OH) and hydrated Electron (e_{aq}) for enhanced radiolytic degradation of 4-nitrophenol by addition of H_2O_2, Enoviron. Sci. Technol. Water 4 (2024) 5077–5088.
[45] K. Liu, F.A. Roddick, L.H. Fan, Impact of salinity and pH on the UVC/H_2O_2 treatment of reverse osmosis concentrate produced from municipal wastewater reclamation, Water Res. 46 (2012) 3229–3239.
[46] J. Ballesteros-Soberanas, C. Bilanin, A. Leyva-Pérez, Parametrization of catalytic organic reactions with convex hammett plots, Acs Org. Inorg. Au 3 (2023) 13–18.

[47] W.H. Tan, W. Ren, C.J. Wang, Y.R. Fan, B. Deng, H. Lin, H. Zhang, Peroxymonosulfate activated with waste battery-based Mn-Fe oxides for pollutant removal: Electron transfer mechanism, selective oxidation and LFER analysis, Chem. Eng. J. 394 (2020) 124864.
[48] L.P. Hammett, The effect of structure upon the reactions of organic compounds. benzene derivatives, J. Am. Chem. Soc. 59 (1937) 96–103.
[49] J.K. Lin, K.S. Hu, Y.T. Wang, W.J. Tian, T. Hall, X.G. Duan, H.Q. Sun, H.Y. Zhang, E. Cortés, S.B. Wang, Tandem microplastic degradation and hydrogen production by hierarchical carbon nitride-supported single-atom iron catalysts, Nat. Commun. 15 (2024).
[50] Z. Wang, W. Qiu, S.Y. Pang, Q. Guo, C.T. Guan, J. Jiang, Aqueous Iron(IV)-oxo complex: an emerging powerful Reactive oxidant formed by Iron(II)-based advanced oxidation processes for oxidative water treatment, Environ. Sci. Technol. 56 (2022) 1492–1509.
[51] Y. Yin, M. Li, X. Li, W. Zhang, L. Lv, J. Wan, Y. Wang, Heterogeneous Fe(IV)=O mediated Fenton-like process on Fe-Zr heterojunction for selective oxidation of organic pollutants at near neutral pH, Chem. Eng. J. 454 (2023) 140516.
[52] J.B. Gordon, T. Albert, A. Dey, S. Sabuncu, M.A. Siegler, E. Bill, P. Moënne-Loccoz, D.P. Goldberg, A. Reactive, Photogenerated high-spin (S= 2) Fe^{IV}(O) complex via O_2 activation, J. Am. Chem. Soc. 143 (2021) 21637–21647.
[53] Y. Lin, Y. Wang, Z. Weng, Y. Zhou, S. Liu, X. Ou, X. Xu, Y. Cai, J. Jiang, B. Han, Z. Yang, Coordination engineering of heterogeneous high-valent Fe(IV)-oxo for safe removal of pollutants via powerful Fenton-like reactions, Nat. Commun. 15 (2024) 10032.
[54] W. Ren, G. Nie, P. Zhou, H. Zhang, X. Duan, S. Wang, The intrinsic nature of persulfate activation and N-doping in carbocatalysis, Environ. Sci. Technol. 54 (2020) 6438–6447.
[55] R.X. Deng, F. Liu, S.X. Gao, Z.W. Xia, R.J. Wu, J.C. Kong, J. Yang, J.H. Wen, X. Zhang, C.D. Lv, Y.H. Wang, X.G. Li, Z. Wang, Rational design of β-MnO_2 via Ir/Ru co-substitution for enhanced oxygen evolution reaction in acidic media, ACS Catal. 15 (2025) 1782–1794.
[56] W. Ren, L.L. Xiong, G. Nie, H. Zhang, X.G. Duan, S.B. Wang, Insights into the Electron-transfer regime of peroxydisulfate activation on carbon nanotubes: the role of oxygen functional groups, Environ. Sci. Technol. 54 (2020) 1267–1275.
[57] W. Ren, C. Cheng, P.H. Shao, X.B. Luo, H. Zhang, S.B. Wang, X.G. Duan, Origins of Electron-transfer regime in persulfate-based nonradical oxidation processes, Environ. Sci. Technol. 56 (2022) 78–97.
[58] D. Su, B.W. Feng, P.F. Xu, Q. Zeng, B.X. Shan, Y.G. Song, Covalent organic frameworks and electron mediator-based open circuit potential biosensor for electrochemical measurements, Anal. Methods-Uk 10 (2018) 4320–4328.
[59] J.F. Yu, L. Tang, Y. Pang, G.M. Zeng, H.P. Feng, J.J. Zou, J.J. Wang, C.Y. Feng, X. Zhu, X.L. Ouyang, J.S. Tan, Hierarchical porous biochar from shrimp shell for persulfate activation: A two-electron transfer path and key impact factors, Appl. Catal. B-Environ. 260 (2020).
[60] K. Wang, T. Zhao, N.Q. Ren, S.H. Ho, Asymmetric defective sites-mediated high-valent cobalt-oxo species in self-suspension aerogel platform for efficient peroxymonosulfate activation, Water Res. 265 (2024).
[61] C. Feng, X.H. She, Y.Q. Xiao, Y.B. Li, Direct detection of Fe^{VI} water oxidation intermediates in an aqueous solution, Angew. Chem. Int. Ed. 62 (2023) 202218738.
[62] J.S. Zhang, W.J. Wei, X.Y. Lu, H. Yang, Z.Q. Chen, R.Z. Liao, G.C. Yin, Nonredox metal ions promoted olefin epoxidation by Iron(II) complexes with H_2O_2: DFT calculations reveal multiple channels for oxygen transfer, Inorg. Chem. 56 (2017) 15138–15149.
[63] J. Chen, A. Draksharapu, D. Angelone, D. Unjaroen, S.K. Padamati, R. Hage, M. Swart, C. Duboc, W.R. Browne, H_2O_2 oxidation by Fe^{III}-OOH intermediates and its effect on catalytic efficiency, ACS Catal. 8 (2018) 9665–9674.
[64] C. Luo, M. Sadhasivan, J. Kim, V.K. Sharma, C.H. Huang, Revelation of Fe(V)/Fe (IV) involvement in the Fe(VI)-ABTS system: kinetic modeling and product analysis, Environ. Sci. Technol. 55 (2021) 3976–3987.
[65] J.K. Norskov, F. Abild-Pedersen, F. Studt, T. Bligaard, Density functional theory in surface chemistry and catalysis, P Natl. Acad. Sci. USA 108 (2011) 937–943.
[66] R.D. Su, Y.X. Gao, L. Chen, Y. Chen, N. Li, W. Liu, B.Y. Gao, Q. Li, Utilizing the oxygen-atom trapping effect of Co_3O_4 with oxygen vacancies to promote chlorite activation for water decontamination, P Natl. Acad. Sci. USA 121 (2024) 2319427121.